

Bayesian Lesion Estimation with a Structured Spike-and-Slab Prior

Anna Menacher¹, Thomas E. Nichols², Chris Holmes¹, and Habib Ganjgahi^{*1,2}

¹Department of Statistics, University of Oxford

²Nuffield Department of Population Health, University of Oxford

June 22, 2022

Abstract

Neural demyelination and brain damage accumulated in white matter appear as hyperintense areas on MRI scans in the form of lesions. Modeling binary images at the population level, where each voxel represents the existence of a lesion, plays an important role in understanding aging and inflammatory diseases. We propose a scalable hierarchical Bayesian spatial model, called BLESS, capable of handling binary responses by placing continuous spike-and-slab mixture priors on spatially-varying parameters and enforcing spatial dependency on the parameter dictating the amount of sparsity within the probability of inclusion. The use of mean-field variational inference with dynamic posterior exploration, which is an annealing-like strategy that improves optimization, allows our method to scale to large sample sizes. Our method also accounts for underestimation of posterior variance due to variational inference by providing an approximate posterior sampling approach based on Bayesian bootstrap ideas and spike-and-slab priors with random shrinkage targets. Besides accurate uncertainty quantification, this approach is capable of producing novel cluster size based imaging statistics, such as credible intervals of cluster size, and measures of reliability of cluster occurrence. Lastly, we validate our results via simulation studies and an application to the UK Biobank, a large-scale lesion mapping study with a sample size of 40,000 subjects.

Keywords: Brain imaging, Variational inference, Spatial statistics, Bayesian bootstrap, Variable selection

*Please address any correspondence to habib.ganjgahi@stats.ox.ac.uk.

1 Introduction

1.1 Motivation for Analysis of White Matter Hyperintensities

Magnetic resonance imaging (MRI) is a non-invasive imaging technique to study human brain structure and function. Accumulated damages to the white matter, known as lesions, appear as localized hypo-/ hyperintensities in MRI scans (Wardlaw et al., 2013). The total burden of these lesions is often associated with cognitive disorders, aging and cerebral small vessel disease, which includes microbleeds, small infarcts and brain atrophy (Wardlaw et al., 2013, 2015). Lesion prevalence is higher for older adults (Griffanti et al., 2018) and in particular for individuals with cerebrovascular risk factors, such as hypertension, alcohol consumption or smoking history (Rostrup et al., 2012; Veldsman et al., 2020). White matter lesions are also an overall indicator of poor brain health and have been found to triple the risk of stroke and double the risk of dementia and death (Debette and Markus, 2010). Not all white matter lesions however are attributed to aging or an increased cerebrovascular risk burden. For example, the inflammatory disease multiple sclerosis causes neuronal demyelination, where the protective layer around the nerves is repeatedly damaged and white matter lesions are able to form. White matter hyperintensities can also occur due to the neurodegenerative disease Alzheimer’s or as a result of a stroke (Debette and Markus, 2010; Prins and Scheltens, 2015). An important clinical feature is the spatial location of lesions; however, the lesions exhibit a high level of variability, together with the size and number of lesions, for both between and within subjects, as seen in the binary lesion masks in Figure 1. Identifying spatial locations in the brain where lesion incidence is associated with different covariates (e.g. age, disease duration or severity) is known as lesion mapping and helps us to get a better understanding on the process of aging and diseases (Veldsman et al., 2020).

1.2 Mass-univariate Methods and Other Spatial Models

The standard practice for lesion mapping is mass-univariate. In this approach a regression model is fitted at each voxel or spatial location independently, any form of spatial dependence among neighboring locations is ignored and multiple testing adjustments are required. Additionally, some authors neglect the binary nature of the lesion data and sim-

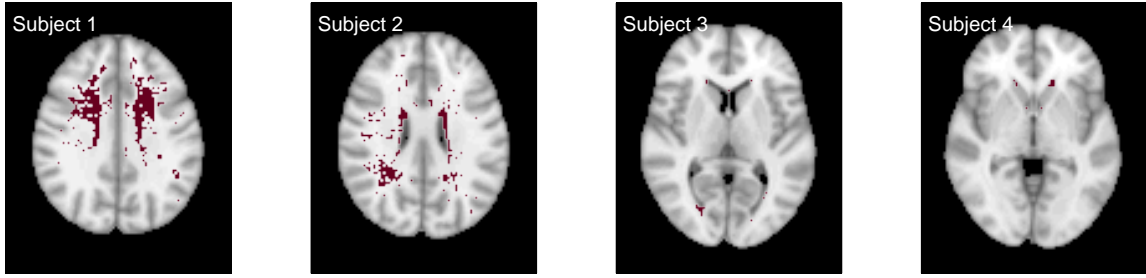


Figure 1: Binary lesion masks from four healthy subjects from the UK Biobank with varying lesion numbers and sizes, where red indicates a lesion at a particular voxel, show the heterogeneity of lesion incidence at various 2D axial slices from the 3D lesion mask.

ply use a voxelwise linear regression between lesion incidence and clinical disability scores (Charil et al., 2003). Other studies respect the binary nature of the output by modeling a voxelwise logistic or probit regression (Rostrup et al., 2012; Lampe et al., 2019). However, they fail to address the problem of complete separation which often occurs in logistic regression models when the output variable separates a subject-specific predictor variable or a combination of input features perfectly and hence leads to infinite and biased maximum-likelihood estimates (Firth, 1993). This problem can be addressed with a logistic regression approach known as Firth Regression, which utilizes a penalized likelihood approach and produces mean-bias reduced parameter estimates (Firth, 1993; Kosmidis et al., 2020).

Bayesian spatial models on the other hand are capable of accounting for the spatial dependence structure among neighboring voxels in a single multivariate model. For example, Ge et al. (2014) have developed a Bayesian spatial generalized linear mixed model (BSGLMM) which performs lesion mapping by associating lesion incidence with subject specific covariates. A smoothing prior, specifically a conditional autoregressive model prior, is placed on the spatially-varying random effect parameters in order to respect the spatial dependence within the data (Besag, 1974, 1993; Mardia, 1988). Unlike this particular Bayesian spatial model, we prefer not to smooth the spatially-varying coefficients directly as this may oversmooth the regression coefficients. Furthermore, parameter estimation and inference is performed via Markov Chain Monte Carlo (MCMC) methods which quickly becomes infeasible for increasing sample sizes. We address the computational complexity of parameter estimation by utilizing alternatives to MCMC sampling, such as variational inference (Blei et al., 2017) and approximate posterior sampling (Nie and Ročková, 2022).

The last decade of brain imaging has brought immense insight into our understanding of

the human brain. However, these findings suffer from small and unrepresentative samples. In addition, environmental and genetic factors that may explain individual differences are ignored which in turn undermines brain related findings. These limitations are being addressed in large-scale epidemiological studies, such as the UK Biobank or the ABCD study, by collecting data on thousands (instead of tens) of subjects. While the main advantage of these data sources lies in their larger sample sizes, they are also beneficial due to their inclusion of multiple high-dimensional imaging modalities as well as recording numerous environmental factors, neurocognitive scores, and other clinical data. The existing methods for brain mapping, specifically lesions, are either simplistic, ignoring complex spatial dependency of intrinsically high-dimensional lesion data, or are not scalable to large-scale studies that can handle the size and complexity of such data.

In order to address the limitations of previous methods, we propose a multivariate Bayesian model for lesion mapping in large-scale epidemiological studies that is (1) capable of handling numerous non-imaging covariates using variable selection and shrinkage priors, (2) takes into account the spatial dependency through a parameter that controls the level of sparsity rather than regression coefficients, and (3) relies on an approximate posterior sampling method based on Bayesian bootstrap techniques rather than MCMC, for parameter estimation and inference. Hence, this allows us to fit the model to thousands of subjects and appropriately account for the spatial dependency in lesion mapping studies containing over 50,000 voxel locations. We also want to acknowledge that other model choices in the literature may better capture the association between lesions and covariates; however, we favor a model that enables us to scale parameter estimation and inference to large-scale epidemiological studies.

1.3 Bayesian Variable Selection

We utilize Bayesian variable selection to improve brain lesion mapping by shrinking small coefficients towards zero, thus helping with prediction, interpretation and reduction of spurious associations in high-dimensional settings. A commonly applied technique for Bayesian variable selection is spike-and-slab regression which aims to identify a selection of predictors within a regression model. The original formulation of the spike-and-slab mixture prior places a mixture of a point mass at zero and a diffuse distribution on the coefficients (Mitchell and Beauchamp, 1988). This approach requires the calculation of poste-

rrior probabilities for all 2^P submodels, where P is the number of covariates. George and McCulloch (1993, 1997) have increased the computational feasibility of spike-and-slab regression problems by introducing a continuous mixture of Gaussian formulation where the spike distribution is defined by a normal distribution with a small variance rather than a point mass prior. Other versions of spike-and-slab priors include non-local prior densities (Johnson and Rossell, 2010), spike-and-slab LASSO priors (Ročková and George, 2018), and global-local priors, such as the horseshoe prior (Carvalho et al., 2009). Overall, the options of continuous shrinkage priors in the literature are large, see Piironen and Vehtari (2017) for a comparison of different methods.

We focus on continuous spike-and-slab priors due to their computationally tractability resulting from the continuity of the spike distribution. Moreover, Bayesian variable selection with traditional spike-and-slab priors relies on MCMC methods whereas shrinkage priors include all covariates in the model and only regularize regression coefficients close to zero (Ročková and George, 2014).

The general setup of a simple normal spike-and-slab regression, modeling the association between a set of covariates $\mathbf{X} \in \mathbb{R}^{N \times P}$ and a dependent variable $\mathbf{y} \in \mathbb{R}^N$ via unknown parameters $\boldsymbol{\beta} \in \mathbb{R}^P$, is typically described by:

$$\begin{aligned}\mathbf{y}|\boldsymbol{\beta}, \sigma^2 &\sim \mathcal{N}(\mathbf{X}\boldsymbol{\beta}, \sigma^2 \mathbf{I}) \\ \boldsymbol{\beta}|\boldsymbol{\gamma} &\sim \mathcal{N}(\mathbf{0}, \mathbf{D}_{\boldsymbol{\gamma}}) \\ \gamma_p|\theta &\stackrel{\text{iid}}{\sim} \text{Bernoulli}(\theta),\end{aligned}$$

where the diagonal matrix is $\mathbf{D} = \sigma^2 \text{diag}\{a_1, \dots, a_P\}$ in the conjugate setting and $\mathbf{D} = \text{diag}\{a_1, \dots, a_P\}$ in the non-conjugate setting of a spike-and-slab mixture prior with $a_p = (1 - \gamma_p)\nu_0 + \gamma_p\nu_1$ and the residual variance σ^2 (George and McCulloch, 1997). The introduction of the binary latent variable $\boldsymbol{\gamma} = (\gamma_1, \dots, \gamma_P)^T$, drawn iid from a Bernoulli distribution with an inclusion probability $\theta \in \mathbb{R}$, hereby enables the identification of high-probability subsets of predictors. Concretely, variable selection is performed by including the variable \mathbf{x}_p in the model and estimating β_p with a non-zero value if $\gamma_p = 1$ and excluding variable \mathbf{x}_p if $\gamma_p = 0$ (George and McCulloch, 1993). In summary, spike-and-slab regression is able to selectively shrink negligible coefficients to zero while leaving the larger parameters unaffected. The amount of regularization is determined by the spike and slab

variance of the Gaussian mixture prior ν_0 and ν_1 , respectively. Using cross-validation for hyperparameter selection over a two-dimensional grid of spike and slab variances is an extremely computationally costly process for high-dimensional models. Dynamic posterior exploration (DPE), developed by Ročková and George (2014), on the other hand avoids applying cross-validation and performs an annealing-like strategy to guide the optimization in their deterministic approach for parameter estimation and inference in spike-and-slab regressions.

1.3.1 Spatial Spike-and-Slab Regression

The spike-and-slab regression is also able to incorporate spatial information, replacing the exchangeable Bernoulli prior on the inclusion variables γ , with a structured spatial prior using a vector of inclusion probabilities $\theta \in \mathbb{R}^P$. Previous examples of introducing structure within a spike-and-slab regression include the placement of a logistic regression product prior (Stingo et al., 2010) on $\gamma|\theta$ in order to group biological information for a genetics application. Another example of a structured prior is the usage of an Ising prior on the latent variables γ to incorporate structural information for a high-dimensional genomics application (Li and Zhang, 2010). Andersen et al. (2014) and Andersen (2017) on the other hand have developed a new class of structured spike-and-slab distributions which model sparsity by placing a spatial Gaussian process on the sparsity parameter θ within the inclusion probabilities $\phi(\theta)$ of the spike-and-slab prior. Note that they do not place a structured prior on the probability of inclusion directly but rather on a sparsity parameter θ and then ensure values between 0 and 1 as inclusion probabilities by transforming θ with a suitable injective function $\phi(\cdot)$. We combine some of these approaches by utilizing the logistic regression prior approach by Stingo et al. (2010) and by placing a spatial prior on the sparsity parameter θ which influences the probability of inclusion or exclusion of a variable. Specifically, we choose a multivariate pairwise difference prior, an instance of a multivariate conditional autoregressive (MCAR) prior, to account for the spatial dependence within the neuroimaging data (Gelfand and Vounatsou, 2003). Furthermore, we avoid an Ising prior on the binary latent indicators which often exhibits the issue of phase transitions. As noted by Ročková and George (2014) and Li and Zhang (2010), the occurrence of phase transitions, especially when the sparsity parameters exhibit a complex spatial structure, is problematic because they introduce a drastic change in the amount of active voxels due to

only a very small change in the hyperparameter configuration.

1.4 Approximate Posterior Inference and Sampling

The gold standard of parameter estimation and inference for spike-and-slab regression with a continuous mixture of Gaussian prior on the coefficients is Gibbs sampling as introduced by George and McCulloch (1993). However, in high-dimensional regression settings as well as large sample size scenarios other more scalable approximate methods for posterior parameter estimation and inference are required due to an intense computational burden and some matrix inversions becoming infeasible.

Expectation propagation (EP) (Minka, 2001) or variational inference (Jordan et al., 1999; Wainwright and Jordan, 2008) algorithms redefine the problem of approximating probability densities through optimization (Blei et al., 2017). Both of these methods have been extensively studied for spike-and-slab regression problems (Hernández-Lobato et al., 2013; Carbonetto and Stephens, 2012). The EP algorithm however poses several challenges as it is computationally intensive for even moderate sample sizes, there is no guarantee of convergence, and its poor performance for multimodal posteriors due to the problematic need to incorporate all modes in its approximation (Bishop, 2006). Poor approximations to the posterior in variational inference can arise due to slow convergence of the optimization problem, a simplistic choice of variational families, or due to underestimation of the posterior variance as the KL-divergence tends to under-penalize thin tails (Blei et al., 2017; Yao et al., 2018).

In neuroimaging applications, however, we require accurate uncertainty estimates of population parameter estimates. Hence, we use approximate posterior sampling methods which capture the marginal posterior density more accurately compared to the more concentrated variational densities. All while remaining highly scalable as their algorithms can be implemented in an embarrassingly parallel manner (Fong et al., 2019). The cornerstone of many of these methods lies in the Bayesian bootstrap (Rubin, 1981). In particular, the Weighted Likelihood Bootstrap (WLB) developed by Newton and Raftery (1994) is a simple approximate posterior sampling method and a special case of many of the more advanced methods developed recently (Fong et al., 2019; Newton et al., 2021; Nie and Ročková, 2022). The WLB approach draws approximate samples from the posterior distribution via randomly re-weighting the likelihood with Dirichlet weights drawn for every

observation in a dataset and then maximizing the re-weighted likelihood with respect to the parameter of interest. Using WLB, Lyddon et al. (2018) and Fong et al. (2019) developed Bayesian nonparametric learning (BNL) routines which utilize parametric models to achieve posterior sampling through the optimization of randomized objective functions; additionally, they do not rely on the traditional assumption of conventional Bayes that the model is true. Therefore, making these methods robust against model misspecification.

Our focus lies on the recently introduced method by Nie and Ročková (2022) which combines Bayesian bootstrap methods with a new class of jittered spike-and-slab LASSO priors with perturbed prior means. This approximate posterior sampling technique performs optimization on many independently perturbed datasets by re-weighting the likelihood as within the WLB by Newton and Raftery (1994) and additionally accounts for the re-weighting of the prior by perturbing the mean of the prior of every covariate with a random shift (Nie and Ročková, 2022). They have also shown that randomly perturbing the prior mean of the marginal spike-and-slab priors introduces a similar effect to the model as if one would have added pseudo-samples from a prior sampling distribution as in the case of BNL (Fong et al., 2019). We argue that for high-dimensional datasets with large samples, where memory allocation is already a computational concern, the approach by Nie and Ročková (2022) is favorable as it merely requires storing an additional set of mean shift parameters compared to an arbitrarily large number of pseudo-samples. Moreover, the approach discussed by Fong et al. (2019) produces exact samples from a posterior by utilizing a weighted EM-algorithm to optimize a pseudo-posterior containing additional pseudo-data drawn from a prior sampling distribution. The exploration of both global and local modes alike ensures that the potentially multimodal posterior landscape is accurately captured. With the link between this method and the work introduced by Nie and Ročková (2022), we hope to incorporate the class of jittered spike-and-slab priors to methods which utilize variational approximations to the posterior for parameter estimation. The variational posterior mean for spike-and-slab priors offers consistency in the frequentist sense. However, it often fails to provide reliable estimates of posterior variances (Blei et al., 2017). We therefore add Bayesian bootstrap methods to capture the posterior variance better.

Another advantage of using bootstrapping techniques is that we can acquire posteriors on complex imaging statistics, such as cluster size. In neuroimaging, a cluster is a contiguous set of voxels with voxelwise statistics that exceed some cluster-defining threshold

(Poline and Mazoyer, 1993). Cluster-wise inference, is declaring clusters significant when they exceed a given size, has been found to be more sensitive to detect true positive effects than voxelwise inference (Friston et al., 1996), albeit having less spatial specificity as the null hypothesis is specified at the level of clusters (Woo et al., 2014). These existing methods can only produce p-values, while we are able to compute credible intervals for cluster size or any other spatial feature of interest by incorporating bootstrapping into our model.

The remainder of this article is organized as follows. In Section 2, we formulate a Bayesian spatial spike-and-slab regression model with approximate posterior sampling via a Bayesian bootstrap procedure, where samples are obtained from a variational approximation using dynamic posterior exploration. In Section 3, we then assess the quality of our method, called BLESS, estimated via variational inference, approximate posterior sampling, and Gibbs sampling, compared to other mass-univariate and Bayesian approaches via simulation studies. The results from the UK Biobank application are given in Section 4. We conclude the paper with a discussion in Section 5 and provide further details on the variational distributions as well as more simulation study results in the supplementary material. Additionally, we make all code publicly available on Github ¹.

2 Methods

Our model for **B**ayesian **L**esion **E**stimation with a **S**tructured **S**pike-and-Slab (**BLESS**) prior is formulated as a Bayesian spatial hierarchical generalized linear model. While we specifically focus on neuroimaging applications within this paper, the model can be applied to any form of spatial binary data on a lattice and can equally be extended to various neuroimaging modalities other than lesion masks.

Throughout this paper we use boldface to indicate a vector or matrix. We model the binary data $y_i(s_j)$ for every subject $i = 1, \dots, N$ at voxel location $s_j \in \mathcal{B} \in \mathbb{R}^3$, $j = 1, \dots, M$, with a Bernoulli random variable with lesion probability $p_i(s_j)$. Due to computational reasons, we choose to model the binary data via a probit link function which defines the relationship between the conditional expectation $\eta_i(s_j)$ and the linear combination of input features \mathbf{x}_i containing P subject-specific covariates, spatially-varying parameters $\boldsymbol{\beta}(s_j)$ and a spatially-varying intercept $\beta_0(s_j)$. While the data comprise an

¹<https://github.com/annamenacher/BLESS>

image for each subject, we store the data as unraveled M -vectors \mathbf{y}_i for each subject or N -vectors $\mathbf{y}(s_j)$ for each voxel.

The Bayesian spatial generalized linear model for subject i at location s_j is specified as

$$[y_i(s_j)|p_i(s_j)] \sim \text{Bernoulli}[p_i(s_j)] \quad (1)$$

$$\Phi^{-1}(p_i(s_j)) = \eta_i(s_j) \quad (2)$$

$$\eta_i(s_j) = \mathbf{x}_i^T \boldsymbol{\beta}(s_j) + \beta_0(s_j), \quad (3)$$

where each equation reflects the random, link and systematic component, respectively and $\Phi(\cdot)$ is the cumulative Gaussian density.

Furthermore, we reformulate the Bayesian probit regression model via the data augmentation approach by Albert and Chib (1993) by introducing latent normal variables into the model in order to ease the computational complexity. This approach assumes that the probit regression has an underlying normal regression structure on latent continuous data. These independent continuous latent variables $z_i(s_j)$ for every subject $i = 1, \dots, N$ and $j = 1, \dots, M$ are drawn from the following normal distribution

$$z_i(s_j)|\eta_i(s_j) \sim \mathcal{N}(\eta_i(s_j), 1) \quad (4)$$

where the conditional probability of $y_i(s_j) = 1$ is given by

$$\Pr[y_i(s_j) = 1|z_i(s_j)] = \begin{cases} 1, & z_i(s_j) > 0, \\ 0, & z_i(s_j) \leq 0. \end{cases} \quad (5)$$

2.1 Prior Specifications

We build a Bayesian hierarchical regression model by placing a continuous version of a spike-and-slab prior on the spatially-varying P -coefficient vector $\boldsymbol{\beta}(s_j)$. The continuous mixture of Gaussians with two different variances, consisting of the spike and the slab distribution, is given by

$$\beta_p(s_j) | \gamma_p(s_j) \sim \mathcal{N}(0, \nu_1 \gamma_p(s_j) + \nu_0 [1 - \gamma_p(s_j)]), \quad (6)$$

where $\gamma_p(s_j)$ is a latent binary indicator variable for covariate $p = 1, \dots, P$ and locations $j = 1, \dots, M$, ν_0 is the spike variance and ν_1 is the slab variance. Variable selection is implemented via the latents $\gamma_p(s_j)$, and specifically it localizes the spatial effect of each variable. Due to the continuous spike-and-slab specification, the variance within the spike distribution is always $\nu_0 > 0$ which ensures the continuity of the spike distribution and therefore the derivation of closed form solutions of the variational parameter updates. The slab variance on the other hand is a set to a fixed value to include the range of all possible values of the spatially-varying coefficients. Particularly, the combination of a small spike variance and a large slab variance with latent indicator variables for every covariate $p = 1, \dots, P$ and location $j = 1, \dots, M$ introduces a selective spatial shrinkage property that shrinks smaller coefficients close to zero and leaves the large parameters unaffected.

In order to account for the spatial dependence across the brain, we place an independent logistic regression prior with non-exchangeable inclusion probabilities on the latent binary indicator variables $\gamma(s_j)$, similar to Stingo et al. (2010). The prior is non-exchangeable because we incorporate structural information via the sparsity parameter $\boldsymbol{\theta}(s_j) \in \mathbb{R}^P$ which ensures that certain voxel locations are more likely to be included in the model than others. In the context of brain imaging data this means that voxels that are nearby each other probably have a similar inclusion probability. Specifically,

$$\gamma_p(s_j) \mid \boldsymbol{\theta}_p(s_j) \sim \text{Bernoulli}(\sigma[\boldsymbol{\theta}_p(s_j)]), \quad (7)$$

where $\sigma(\cdot)$ is a sigmoid function, and the P -vector $\boldsymbol{\gamma}(s_j)$ has the probability mass function

$$\pi(\boldsymbol{\gamma}(s_j) \mid \boldsymbol{\theta}(s_j)) = \prod_{p=1}^P \left(\frac{\exp(\boldsymbol{\theta}_p(s_j))}{1 + \exp(\boldsymbol{\theta}_p(s_j))} \right)^{\gamma_p(s_j)} \left(\frac{1}{1 + \exp(\boldsymbol{\theta}_p(s_j))} \right)^{1 - \gamma_p(s_j)}. \quad (8)$$

The hierarchical spatial regression model is completed by placing a spatial prior on the sparsity parameter $\boldsymbol{\theta}^T = [\boldsymbol{\theta}^T(s_1), \dots, \boldsymbol{\theta}^T(s_M)]$: a length PM column vector. We choose a multivariate conditional autoregressive (MCAR) prior as a spatial prior due to computational reasons (Gelfand and Vounatsou, 2003). Alternative priors could be considered in lieu of this type of a simple smoothing prior; however, this would significantly increase the computational complexity of the model at hand.

The full conditional distribution for $\boldsymbol{\theta}(s_j)$ is given by the following multivariate normal

distribution and utilizes the notation defined by Mardia (1988):

$$[\boldsymbol{\theta}(s_j) \mid \boldsymbol{\theta}(-s_j), \boldsymbol{\Sigma}^{-1}] \sim \text{MVN} \left(\frac{\sum_{s_r \in \partial s_j} \boldsymbol{\theta}(s_r)}{n(s_j)}, \frac{\boldsymbol{\Sigma}}{n(s_j)} \right), \quad (9)$$

where $\boldsymbol{\Sigma}$ is a symmetric positive definite smoothing matrix. The sum $\sum_{s_r \in \partial s_j}$ defines the sum over the neighborhood voxels at location s_j , ∂s_j defines the set of neighbors at location s_j and $n(s_j)$ is the cardinality of the neighborhood set. For our MRI scans we consider only neighbors sharing a face, so therefore most of the interior of the brain has $n(s_j) = 6$ neighbors whereas locations near the brain mask have $n(s_j) < 6$.

We then describe the joint distribution over the sparsity parameters, up to a proportionality constant, by utilizing Brooks's lemma (Brook, 1964) which is given by:

$$\pi(\boldsymbol{\theta} \mid \boldsymbol{\Sigma}) \propto \exp \left\{ -\frac{1}{2} \sum_{s_j \sim s_{j'}} [\boldsymbol{\theta}(s_j) - \boldsymbol{\theta}(s_{j'})]^T \boldsymbol{\Sigma}^{-1} [\boldsymbol{\theta}(s_j) - \boldsymbol{\theta}(s_{j'})] \right\}, \quad (10)$$

where the sum $\sum_{s_j \sim s_{j'}}$ describes the sum over neighborhood voxels, and $s_j \sim s_{j'}$ indicates that s_j and $s_{j'}$ are neighbors. This joint prior distribution is improper and not identifiable according to Besag (1986). However, the posterior of $\boldsymbol{\theta}$ is proper, if there is information in the data with respect to the sparsity parameters. Lastly, we finish specifying the Bayesian hierarchical regression model by placing an uninformative, conjugate Wishart prior over the precision matrix $\boldsymbol{\Sigma}^{-1}$ to fully specify the model with

$$\boldsymbol{\Sigma}^{-1} \sim \text{Wishart}(\nu, \mathbf{I}), \quad (11)$$

where the degrees of freedom are given by $\nu = P$ and the scale matrix is defined by the identity matrix \mathbf{I} (Ge et al., 2014).

2.2 Posterior Approximation

The first element of our scalable approximate posterior sampling approach is a variational approximation to the posterior using optimization instead of MCMC sampling. Hence, every sample within the approach, as defined in Section 2.4, is acquired by optimizing the posterior via variational inference. We opt for variational inference due to the non-conjugacy in the hierarchical model induced by specifying a logistic function around the

sparsity parameters $\boldsymbol{\theta}$ in the probabilities of inclusion of the spike-and-slab priors. Local variational approximations solve this problem by finding a bound on an individual set of variables via a first-order Taylor approximation (Jaakkola and Jordan, 2000). For general variational inference, we then require the full joint distribution of the Bayesian spatial regression model, consisting of the likelihood $p(\mathbf{Y}|\mathbf{X}, \boldsymbol{\beta}, \boldsymbol{\beta}_0)$ and the joint prior $p(\mathbf{Z}, \boldsymbol{\beta}, \boldsymbol{\beta}_0, \boldsymbol{\gamma}, \boldsymbol{\theta}, \boldsymbol{\Sigma}^{-1})$, which is given by

$$p(\mathbf{Y}, \mathbf{Z}, \mathbf{X}, \boldsymbol{\beta}, \boldsymbol{\beta}_0, \boldsymbol{\gamma}, \boldsymbol{\theta}, \boldsymbol{\Sigma}^{-1}) = p(\mathbf{Y}|\mathbf{Z})p(\mathbf{z}|\mathbf{X}, \boldsymbol{\beta}, \boldsymbol{\beta}_0)p(\boldsymbol{\beta}_0)p(\boldsymbol{\beta}|\boldsymbol{\gamma})p(\boldsymbol{\gamma}|\boldsymbol{\theta}) \quad (12)$$

$$p(\boldsymbol{\theta}|\boldsymbol{\Sigma}^{-1})p(\boldsymbol{\Sigma}^{-1}).$$

We write the entire set of model parameters as $\boldsymbol{\Psi} = \{\mathbf{Z}, \boldsymbol{\beta}, \boldsymbol{\beta}_0, \boldsymbol{\gamma}, \boldsymbol{\theta}, \boldsymbol{\Sigma}^{-1}\}$ where the conditional distribution of each model parameter $\boldsymbol{\psi}$ is obtained as $p(\boldsymbol{\psi}|\mathbf{y}) = \frac{p(\boldsymbol{\psi}, \mathbf{y})}{p(\mathbf{y})}$. We acquire an approximation to the exact posterior by firstly specifying a family of densities \mathcal{Q} over each model parameter $\boldsymbol{\psi}$ and secondly identifying the parameter setting of the candidate distribution $q(\boldsymbol{\psi}) \in \mathcal{Q}$ that minimizes the Kullback-Leibler (KL) divergence, given by

$$q^*(\boldsymbol{\psi}) = \arg \min_{q(\boldsymbol{\psi}) \in \mathcal{Q}} \text{KL} (q(\boldsymbol{\psi}) || p(\boldsymbol{\psi}|\mathbf{y})). \quad (13)$$

We aim to minimize the difference between the exact posterior $p(\boldsymbol{\psi}|\mathbf{y})$ and the variational distribution $q(\boldsymbol{\psi})$ in order to find the best approximate distribution $q^*(\boldsymbol{\psi})$. However, rather than computing the KL-divergence which contains the log-marginal of the data, a quantity that is not computable most of the time, we optimize the so-called evidence lower bound (ELBO). The ELBO is an alternative optimization objective which consists of the negative KL-divergence and an added constant, the logarithm of the evidence $p(\mathbf{y})$. Therefore, minimizing the KL-divergence is equivalent to maximizing the ELBO (Blei et al., 2017).

The evidence lower bound for BLESS is defined via Jensen's inequality (Jordan et al., 1999) by

$$\mathcal{L}(q) \geq \mathbb{E}_{q(\mathbf{Z}, \boldsymbol{\beta}, \boldsymbol{\beta}_0, \boldsymbol{\gamma}, \boldsymbol{\theta}, \boldsymbol{\Sigma}^{-1})} [\ln \{p(\mathbf{Y}, \mathbf{Z}, \mathbf{X}, \boldsymbol{\beta}, \boldsymbol{\beta}_0, \boldsymbol{\gamma}, \boldsymbol{\theta}, \boldsymbol{\Sigma}^{-1})\}] - \quad (14)$$

$$\mathbb{E}_{q(\mathbf{Z}, \boldsymbol{\beta}, \boldsymbol{\beta}_0, \boldsymbol{\gamma}, \boldsymbol{\theta}, \boldsymbol{\Sigma}^{-1})} [\ln \{q(\mathbf{Z}, \boldsymbol{\beta}, \boldsymbol{\beta}_0, \boldsymbol{\gamma}, \boldsymbol{\theta}, \boldsymbol{\Sigma}^{-1})\}]. \quad (15)$$

The derivation of the variational distributions of the model parameters in the set $\boldsymbol{\Psi}$

as well as the derivation of the ELBO can be found in supplementary material in Section 2.2 and 2.3 respectively. After determining the variational distributions q , we successively update each parameter ψ , while holding the others fixed, via mean-field coordinate ascent variational inference (Bishop, 2006). With this procedure, the ELBO continuously increases until the algorithm converges to a local optimum when the difference in ELBO between two consecutive steps reaches a pre-determined convergence threshold ϵ . It should be noted that variational inference is also sensitive to parameter initialization considering the highly non-convex nature of the optimization problem. Hence, we choose to initialize β and β_0 with estimates obtained by the mass-univariate approach Firth regression, γ with the fixed value 0.5, θ with the logit transformed fraction of active voxels for every covariate from Firth regression, and Σ^{-1} with an identity matrix in order to ensure convergence to a local optimum.

2.3 Dynamic Posterior Exploration

Dynamic posterior exploration (DPE) (Ročková and George, 2014), is an annealing-like strategy, which fixes the slab variance to a large, fixed value. The procedure works by starting in a smooth posterior landscape and aims to discover a sparse, multimodal posterior by gradually decreasing the value of the spike parameter until it approximates the spike-and-slab point mass prior. Hence, in the beginning we should be able to easily identify a small set of local optima by maximizing the ELBO when the starting spike variance is large. Thereafter, the technique uses the result as a warm start for the next optimization with a reduced spike variance which leads to a more peaked posterior until the last value within a range of spike variances is evaluated and a stable solution to the optimization problem is found.

The process of dynamic posterior exploration can be split into three parts. Firstly, we perform parameter estimation via variational inference over a sequence of K increasing spike variances $\nu_0 \in V = \{\nu_0^{(1)}, \dots, \nu_0^{(K)}\}$. The starting value of the backwards DPE procedure $\nu_0^{(K)} \leq \nu_1$ is run first, and then after initializing the parameters when $\nu_0^{(K)}$, every subsequent optimization is run with a successively smaller ν_0 and initialized with the previously estimated variational parameters as a “warm start” solution. Secondly, the output of every optimization run within the sequence of spike parameter values V is thresholded via the posterior inclusion probabilities. The thresholding rule for BLESS is

based on the following inclusion probabilities

$$\hat{\gamma}_p(s_j) = \begin{cases} 1, & \text{if } P(\gamma_p(s_j) = 1 | \mathbf{Y}, \hat{\boldsymbol{\beta}}, \hat{\boldsymbol{\beta}}_0, \hat{\boldsymbol{\theta}}) > 0.5, \\ 0, & \text{if } P(\gamma_p(s_j) = 1 | \mathbf{Y}, \hat{\boldsymbol{\beta}}, \hat{\boldsymbol{\beta}}_0, \hat{\boldsymbol{\theta}}) \leq 0.5, \end{cases} \quad (16)$$

which is equivalent to the local version of the median probability model defined by Barbieri et al. (2021). Furthermore, the determination of active versus inactive voxels based on the inclusion probability $P(\gamma_p(s_j) = 1 | \mathbf{y})$ is equivalent to thresholding the parameter estimates $\hat{\boldsymbol{\beta}}$ themselves where the threshold is given by the intersection of the weighted mixture of the spike-and-slab priors (George and McCulloch, 1993; Ročková and George, 2014). For BLESS, we choose the former thresholding rule based on the posterior inclusion probabilities considering that thresholding the parameters $\hat{\boldsymbol{\beta}}$ would require the calculation of a different set of intersection points for every coefficient due to the non-exchangeable nature of the spatial prior within the inclusion probability. Thirdly, the estimated posterior with the smallest spike variance ν_0 within the range of parameters V is used. We do not assert that this ν_0 is optimal per se, but that our annealing-like strategy obviates the need for a precise determination of ν_0 as the estimates for the larger effects tend to stabilize at a particular solution of variational posterior parameters.

This behavior can be validated by two types of plots. Regularization plots enable the examination of the estimated coefficients over a sequence of spike variances. For each ν_0 , the color of the parameter values indicates whether or not a variable is included in (red) or excluded from (blue) the model based on the thresholded posterior probability of inclusion. Figure 2(a) illustrates how the negligible coefficients are drawn to zero as the values of ν_0 decrease, while the larger parameters of the active voxels stabilize and are unaffected by regularization. Hence, for the plot in Figure 2(a) this occurs at a log-spike variance $\log(\nu_0) \leq -6$ where the potentially global optimum has been identified and any further decrease in spike variance only leads to further shrinkage of the negligible coefficients in order to approximate the point mass prior.

A complementary plot, especially useful when overplotting makes the regularization plot difficult to interpret, is the log-marginal posterior plot $\ln\{\pi_{\nu_0=0}(\boldsymbol{\gamma} | \mathbf{y}, \boldsymbol{\theta}, \boldsymbol{\Sigma}^{-1})\}$ for the latents. The maximum value of this quantity yields the posterior closest to approximating the point mass prior which is the goal of backwards DPE. Since our model contains

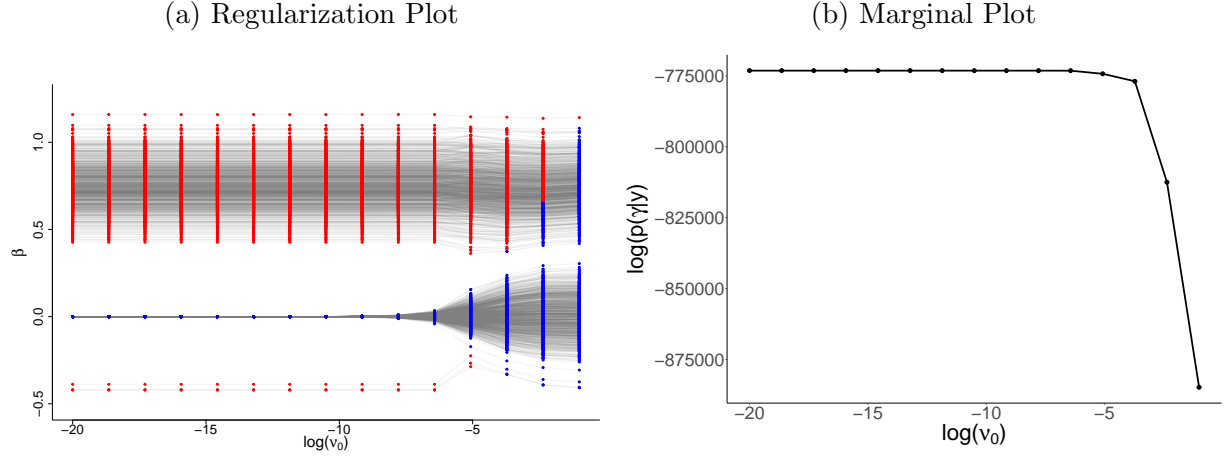


Figure 2: (a) Regularization plot (active voxel: red, inactive voxel: blue) and (b) plot of marginal posterior of $\hat{\gamma}$ under $\nu_0 = 0$ over a sequence of equidistant $\nu_0 \in V$ within log-space for the simulation study described in Section 3 for sample size $N = 1,000$ and base rate intensity $\lambda = 3$. Both plots indicate that parameter estimates have stabilized past spike variances of $\log(\nu_0) \leq -6$ within the DPE procedure. The regularization plot also shows how negligible (blue) coefficients are progressively shrunk towards 0 while the larger (red) coefficients remain almost unregularized.

intractable integrals, we use a variational approximation to the marginal posterior of γ under the prior of $\nu_0 = 0$. We utilize Jensen's inequality to bound the marginal probability integrating out the parameters β , β_0 and the latent variables \mathbf{Z} via their respective variational approximation. The other model parameters θ and Σ^{-1} are regarded as nuisance parameters. Specifically, the log-marginal posterior under $\nu_0 = 0$ and its approximation

$$\ln\{\pi_{\nu_0=0}(\gamma|\mathbf{Y}, \theta, \Sigma^{-1})\} \quad (17)$$

$$= \ln \left\{ \int \int \int q(\mathbf{Z}, \beta_\gamma, \beta_0) \frac{p(\mathbf{Y}, \mathbf{Z}, \beta_\gamma, \beta_0, \gamma, \theta, \Sigma^{-1} | \mathbf{X}_\gamma)}{q(\mathbf{Z}, \beta_\gamma, \beta_0)} d\mathbf{Z} d\beta_\gamma d\beta_0 \right\} \quad (18)$$

$$\geq \mathbb{E}_{q(\mathbf{Z}, \beta_\gamma, \beta_0)} [\ln \{p(\mathbf{Y}, \mathbf{Z}, \beta_\gamma, \beta_0, \gamma, \theta, \Sigma^{-1} | \mathbf{X}_\gamma)\}] - \mathbb{E}_{q(\mathbf{Z}, \beta_\gamma, \beta_0)} [\ln \{q(\mathbf{Z}, \beta_\gamma, \beta_0)\}] \quad (19)$$

can be used to determine whether or not the parameters identified as active have stabilized by checking a single quantity rather than the solution path of all parameters of the model. Figure 2(b) illustrates the marginal $\ln\{\pi_{\nu_0=0}(\gamma|\mathbf{y}, \theta, \Sigma^{-1})\}$, showing a plateau for any log-spike variance $\log(\nu_0) \leq -6$ indicating a good approximation of the point mass prior. The marginal plot can be used in an equivalent manner to the regularization plot as a

sanity check for visualizing the stabilization of large effects and continued shrinkage for the negligible coefficients at the end of the annealing-like process.

2.4 Uncertainty Quantification via Bayesian Bootstrap - BLESS with a Jittered Spike-and-Slab Prior

Algorithm 1: BB-BLESS

Result: Sample of parameter estimates $\tilde{\beta}$ from approximate posterior distribution.

Set: $\nu_0 = \nu_0^{DPE}$; ν_1 : large, fixed value; α : concentration parameter;

ϵ : convergence criterion; B : number of bootstraps

for $b = 1, \dots, B$ **do**

- 1) Sample weights $\mathbf{w}^{(b)} \sim NDirichlet(\alpha, \dots, \alpha)$.
 - 2) Sample mean shifts $\boldsymbol{\mu}^{(b)}(s_j)$ for all $j = 1, \dots, M$ from $\mu_p(s_j) \sim \mathcal{N}(0, \nu_0)$.
 - 3) Calculate $\tilde{\beta}^{(b)}$ by acquiring variational posterior mean via approximating pseudo-posterior via variational inference.
-

We use Bayesian bootstrapping techniques (Nie and Ročková, 2022) to obtain approximate posterior samples. The approach for Bayesian Bootstrap - BLESS (BB-BLESS) is threefold and is described by Algorithm 1: Firstly, weights $w_i^{(b)}$ are sampled for every observation $i = 1, \dots, N$ from a Dirichlet distribution, which has been scaled by the sample size N , in order to re-weight the likelihood following the weighted likelihood bootstrap by Newton and Raftery (1994). Every weight $w_i^{(b)}$ hereby perturbs the contribution of each observation to the likelihood. Secondly, a prior mean shift $\mu_p(s_j)$ is sampled for every covariate $p = 1, \dots, P$ and voxel $j = 1, \dots, M$ from the spike distribution. For initialization, the variational parameters estimated when performing DPE for BLESS-VI (BLESS estimated via variational inference alone) at the target spike variance value ν_0 are used as initial values to BB-BLESS. This prior mean shift $\mu_p(s_j)$ is then used to center the prior for $\pi(\beta(s_j)|\gamma(s_j))$ on $\boldsymbol{\mu}(s_j)$ instead of $\mathbf{0}$ (Nie and Ročková, 2022). This combination of Bayesian bootstrap methods and the jittering of the spike-and-slab prior allows for approximate posterior sampling by repeatedly optimizing the updated ELBO with respect to its variational parameters to approximate a posterior density. The variational posteriors for all other nuisance parameters are also re-fitted for every bootstrap sample. Thirdly, we acquire a sample $\tilde{\beta}^{(b)}(s_j)$ by optimizing the ELBO with respect to the spatially-varying

coefficient $\tilde{\beta}^{(b)}(s_j)$. The following is a variational approximation to the pseudo-posterior, defined by a re-weighted likelihood and perturbed prior:

$$q(\tilde{\beta}^{(b)}(s_j)) \propto \exp \left\{ \mathbb{E}_{q(\mathbf{Z}, \beta_0, \gamma, \theta, \Sigma^{-1})} \left[\ln \left\{ \prod_{i=1}^N p(y_i(s_j) | z_i(s_j)) p(z_i(s_j) | \beta(s_j), \beta_0, \mathbf{x}_i)^{w_i^{(b)}} \right. \right. \right. \\ \left. \left. \left. p(\beta(s_j) | \mu(s_j)^{(b)}, \gamma(s_j)) p(\beta_0) p(\gamma | \theta) p(\theta | \Sigma^{-1}) p(\Sigma^{-1}) \right\} \right] \right\}, \quad (20)$$

where the Dirichlet weights are $(w_1^{(b)}, \dots, w_N^{(b)}) \sim \text{Dir}(\alpha, \dots, \alpha)$ and the jitter is drawn via the spike distribution $\mu_p(s_j) \sim \mathcal{N}(0, \nu_0)$. Each bootstrap sample $\tilde{\beta}^{(b)}(s_j)$ is acquired by taking the marginal variational posterior mean of the pseudo-posterior defined in Equation (20) where the nuisance parameters are approximately marginalized out.

3 Simulation Study

In this section, we firstly explain the process of simulating lesion data where the ground truth is known. We perform various simulation studies to assess the performance of BLESS, estimated via variational inference (BLESS-VI), approximate posterior sampling (BB-BLESS) and traditional Gibbs sampling (BLESS-Gibbs), by assessing their marginal posterior distributions and quantities. In addition, we compare parameter estimates and predictive performance of our method to the mass-univariate approach, Firth regression (Firth, 1993), and the Bayesian spatial model, BSGLMM (Ge et al., 2014). For comparison, the latter is adopted to fit a Bayesian hierarchical modeling framework, similar to BLESS, where we add a spatially-varying intercept $\beta_0(s_j)$ to match the setup of BLESS. For Firth regression, which fits an independent probit regression model with a mean bias reduction for every voxel location, we use the *R* package *brglm2* (Kosmidis, 2021).

The main aim of many neuroimaging studies lies in the provision of accurate inference results. We therefore tailor the assessment of simulation studies on the evaluation of inference results rather than on coverage probabilities. We compare inference results by assessing true positive (TP), false positive (FP), true negative (TN), and false negative (FN) discoveries in the following measures: (1) sensitivity/true positive rate ($\text{TPR} = \frac{\text{TP}}{\text{TP} + \text{FN}}$), (2) true discovery rate ($\text{TDR} = \frac{\text{TP}}{\text{TP} + \text{FP}}$), (3) specificity/1 - false positive rate ($\text{FPR} = \frac{\text{FP}}{\text{FP} + \text{TN}}$), and (4) false discovery rate ($\text{FDR} = \frac{\text{FP}}{\text{FP} + \text{TP}}$). Lastly, we provide extensive simulation stud-

ies on the performance of BLESS-VI compared to a frequentist, mass-univariate approach as well as a Bayesian spatial model with a simulation study addressing varying sample sizes N , base rate intensities λ , and sizes of effect within an image. Base rate intensities hereby provide an indicator for the magnitude of various regression coefficient effect sizes where a smaller λ value yields smaller regression coefficients.

For simulating the data, we adopt a data generating process that is different from our model in order to guarantee a fair comparison between the method we propose, BLESS, to the other methods, BSGLMM and Firth regression. We therefore use a data generating mechanism which simulates homogeneous regions of lesions proposed by Ge et al. (2014), with intensities that vary over subjects, which provides us with a tool to provide a fair comparison among the three methods evaluated.

For our study, we consider $P = 2$ effects in addition to an intercept, we label sex and group (e.g. patient and control). We simulate 2-D binary lesion masks of size 50×50 , $M = 2,500$, with homogeneous effects in each 25×25 quadrant. The effect of sex leads to 4 times more lesions on the right side of an image for female subjects compared to the baseline. The second effect of group membership introduces an effect of 4 times more lesions within the lower left quadrant of an image for subjects within group 2. A Poisson random variable with base rate λ determines the number of lesions. Further details and plots of the simulated data can be found in the supplementary materials in Section 5.

3.1 BB-BLESS Simulation Study

In this simulation study on a low base rate and sample size scenario ($N = 500$, $\lambda = 1$) as well as a high base rate and sample size scenario ($N = 1,000$, $\lambda = 3$), we want to assess the performance of BLESS estimated via variational inference (BLESS-VI), approximate posterior sampling (BB-BLESS) and traditional Gibbs sampling (BLESS-Gibbs) on two scenarios with small and large regression coefficients based on their base rate intensity $\lambda = 1$ and $\lambda = 3$. The posterior quantities of BLESS-VI are acquired by running a separate backwards dynamic posterior exploration procedure for every dataset with an equispaced spike sequence of $\nu_0 = \exp\{-20, \dots, -1\}$ of length 15 and a slab variance of $\nu_1 = 10$. The method is initialized with the coefficients of Firth regression where we use the parameter estimates and respective inference results from the final run in the backwards DPE procedure ($\nu_0 = \exp(-20)$). We estimate BB-BLESS by drawing $B =$

1,000 bootstrap replicates and Dirichlet weights with a concentration parameter $\alpha = 1$. We run the Gibbs sampler for 15,000 iterations and discard 5,000 iterations as burn-in. The performance of BB-BLESS and BLESS-Gibbs is then greatly improved by utilizing the output of the backwards DPE procedure as parameter initialization for the respective parameter estimation techniques.

Firstly, we examine the marginal posterior densities of a random active and inactive voxel. As expected, the posterior variance from BLESS estimated via variational inference is underestimated as the posterior distribution is very peaked around the posterior mean (Fig. 3a, b). On the other hand, the posterior estimated via BB-BLESS aligns well with the distribution acquired via the gold standard method of Gibbs sampling. This is further illustrated by comparing the marginal posterior densities of all voxels within an effect image via KL-divergence and Wasserstein distance in Figure 3c, d. Both methods show the higher quality of posterior approximation via BB-BLESS compared to BLESS-VI when calculating the discrepancy of the distributions acquired via approximate methods and Gibbs sampling.

Figure 3 illustrates that both BB-BLESS and BLESS-VI are able to better capture the posterior mean of all voxel locations within an image when compared to BLESS estimated via Gibbs sampling. However, BLESS-VI severely underestimates the posterior standard deviation for both active and inactive voxels. Lastly, we compare the inference results of our method BLESS-VI, where we use the marginal posterior probability of inclusion as a proxy for inference, to the approximate posterior sampling technique BB-BLESS and the gold standard of BLESS-Gibbs, for which we determine activation via test statistics $t = \frac{\hat{\beta}}{\sigma_{\hat{\beta}}}$, for two simulation study setups. BLESS estimated via Gibbs sampling yields high sensitivity and a very low false positive rate for both settings in Table 1. More importantly, the inference results for BB-BLESS and BLESS-VI are very similar, i.e. the false positive rate for both BB-BLESS and BLESS-VI lies at 2.57% for a sample size of $N = 500$ and base rate intensity of $\lambda = 1$. Hence, we showcase empirically that, when it comes to inference, thresholding posterior inclusion probabilities in BLESS-VI yields similar results to the approximate posterior sampling approach BB-BLESS which determines effect detection via test statistics. Hence, if a researcher is uninterested in the additional features of BB-BLESS, such as acquiring uncertainty estimates of coefficients or more complex imaging statistics, then the application of BLESS-VI alone can be considered for parameter estimation and inference, as we get empirically similar voxelwise inference results in our simulation studies

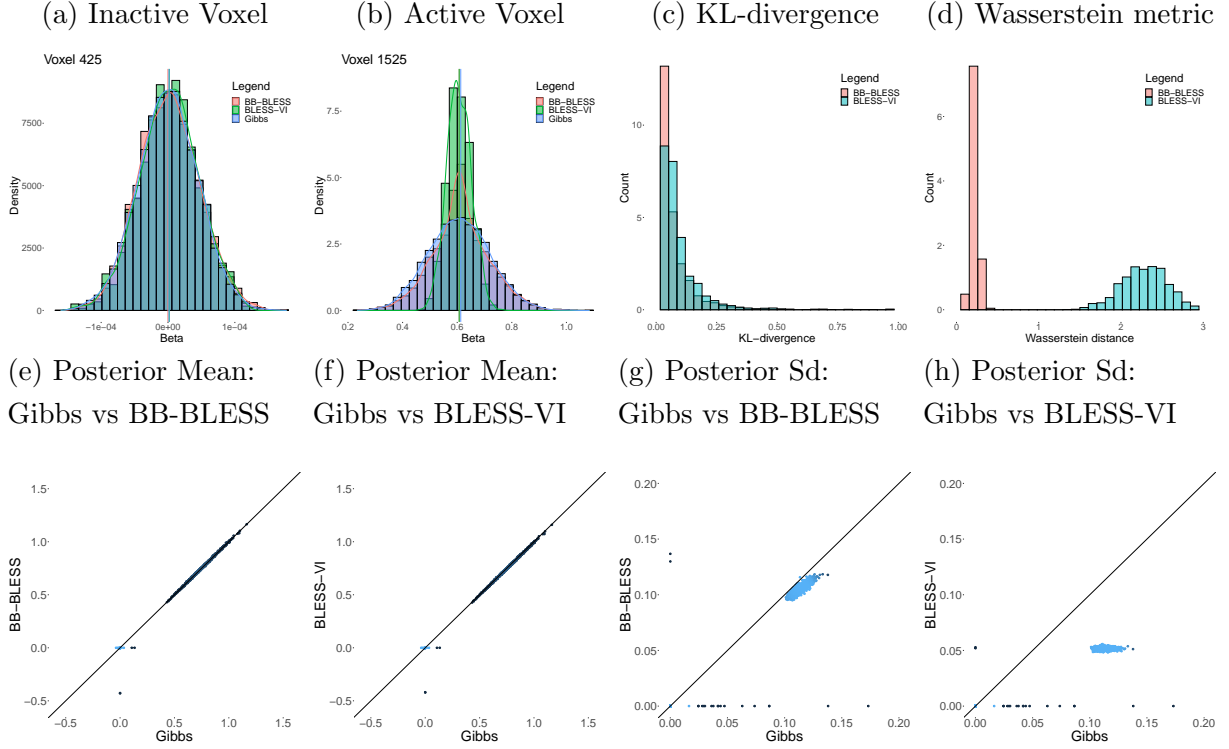


Figure 3: Comparison of marginal posterior distributions for an (a) active and (b) inactive voxel between BB-BLESS, BLESS-Gibbs, and BLESS-VI where the posterior mean is indicated via a vertical line. Overall evaluation of marginal posterior distributions for all voxels between Gibbs and BB-BLESS and BLESS-VI via (c) KL-divergence and (d) Wasserstein distance. Comparison of posterior quantities, such as posterior mean (e)-(f) and standard deviation (g)-(h), of the parameter estimates for all voxels for $N = 1,000$ and $\lambda = 3$ (lighter values indicate higher density of values). Parameters acquired via BLESS-VI exhibit similar point estimates to BB-BLESS and Gibbs but their posterior distributions are too peaked and variances are underestimated.

at a lower overall computational cost for BLESS-VI compared to BB-BLESS.

3.2 BLESS-VI Simulation Study

We extend our simulation study to evaluate the performance of BLESS-VI for a broader set of scenarios with varying sample sizes $N = \{500; 1,000; 5,000\}$, base rate intensities $\lambda = \{1, 2, 3\}$ and sizes of spatial effect, where 25% (group effect) or 50% (sex effect) of the image are active, compared to BSGLM and Firth regression. The true and estimated parameter estimates are available in the supplementary materials alongside more results from simulation studies with different spatial priors and varying magnitudes of the slab

$N = 500$ and $\lambda = 1$					$N = 1,000$ and $\lambda = 3$			
$\hat{\beta}_1$	Bias	Variance	MSE		Bias	Variance	MSE	
BLESS-Gibbs	0.0288	0.0406	0.0414		0.0060	0.0065	0.0065	
BB-BLESS	-0.0857	0.0171	0.0245		0.0078	0.0063	0.0064	
BLESS-VI	-0.1037	0.0013	0.0121		0.0027	0.0010	0.0010	
BSGLMM	0.0518	0.0120	0.0147		0.0126	0.0039	0.0040	
Firth	-0.0182	0.0539	0.0542		-0.0027	0.0118	0.0118	
$t_{\hat{\beta}_1}$	TPR	TDR	FPR	FDR	TPR	TDR	FPR	FDR
BLESS-Gibbs	0.7319	0.9998	0.0001	0.0002	0.9999	0.9999	0.0001	0.0001
BB-BLESS	0.6263	0.9606	0.0257	0.0394	0.9999	0.9970	0.0031	0.0030
BLESS-VI	0.6263	0.9606	0.0257	0.0394	1.0000	0.9970	0.0031	0.0031
BSGLMM	0.9991	0.9004	0.1128	0.0996	1.0000	0.9027	0.1088	0.0973
Firth	0.6566	0.8953	0.0768	0.1047	1.0000	0.9637	0.0379	0.0363

Table 1: Evaluation of parameter estimates and inference results for BLESS (Gibbs, BB, VI), BSGLMM and Firth for two simulation study scenarios ($N = 500$, $\lambda = 1$ and $N = 1,000$, $\lambda = 3$) for the effect of sex. MSE of parameter estimates for BB-BLESS and BLESS-Gibbs are comparable. Inference results from thresholding posterior inclusion probabilities for BLESS-VI and test statistics for BB-BLESS also achieve similar rates.

variance. We will focus on the effect map for the covariate sex and generate 100 datasets for each sample size and base rate scenario to provide robustness by averaging over the results of each dataset. The setup for BLESS-VI is identical to the procedure described in the section above.

The quality of parameter estimates and prediction for BLESS-VI, BSGLMM and Firth regression are evaluated via bias, variance and mean squared error (MSE) in Table 2. BLESS-VI exhibits the lowest bias for the evaluation of the parameter estimates for the sex effect for all levels of base rate intensities and sample sizes compared to BSGLMM and Firth regression. Equally, BLESS outperforms the mass-univariate approach when comparing the quality of the coefficients via MSE. For example, the MSE of the parameter estimates for a small sample size $N = 500$ and low base rate intensity $\lambda = 1$ is approximately 5 times larger for Firth regression with a value of 0.0565 compared to our method BLESS with a value of 0.0106. Hence, this showcases how BLESS adequately regularizes negligible coefficients to zero while the larger effects are unaffected by shrinkage. The quality of the predictive performance is determined by comparing the true empirical lesion rates to the estimated lesion probabilities. BLESS-VI yields slightly better predictive results with respect to MSE, by exhibiting less biased estimates, compared to Firth regression for all scenarios except for the instance with low sample size and base rate intensity ($N = 500$, $\lambda = 1$) where Firth

regression exhibits a slightly lower MSE. This result motivates the usage of BLESS for studies with larger sample sizes where BLESS outperforms the mass-univariate approach.

Our simulation study enforces 50% of the voxels as active on the right side of an image for the covariate sex and 25% of the voxels as active within the lower left quadrant of an image. Hence, by knowing the true location of the effect, we can evaluate the quality of the inference results of BLESS compared to BSGLMM and Firth regression. Effect detection for BLESS is determined by utilizing the binary latent variables $\hat{\gamma}$, marking voxels s_j significant if $P(\gamma_p(s_j) = 1|\mathbf{y}) > 0.5$. For BSGLMM and Firth regression we acquire test statistics $t = \frac{\hat{\beta}}{\sigma_{\hat{\beta}}}$ and threshold them at a significance level of 5%. It should be noted that the latter approaches requires a multiple testing adjustment where the mass-univariate approach in particular ignores any form of spatial dependence. Hence, the p-values are adjusted via a Benjamini-Hochberg procedure (Benjamini and Hochberg, 1995).

All methods have comparable results with respect to their performance in parameter estimation and prediction. However, the evaluation of the inference results in Figure 4 showcases that the Bayesian spatial model BSGLMM has a particularly high number of false positives and hence an incredibly low level of specificity compared to the other methods BLESS-VI and Firth regression. BLESS’s key advantage is therefore shown by comparable levels of sensitivity and high values of specificity for all configurations of sample size and base rate intensity. We note that we see even more pronounced results in favor of BLESS compared to the other methods for lower sizes of effect (group effect at 25% of the image) which can be found in the supplementary materials in Section 7.

4 UK Biobank Application

4.1 Data Description and Processing

Our motivating data set is from the UK Biobank, a large-scale biomedical database containing imaging data from predominately healthy individuals. With a target of 100,000 subjects, there is currently imaging data available for 40,000 participants (Miller et al., 2016). We refer the reader to Miller et al. (2016) and Alfaro-Almagro et al. (2018) for a detailed description of the scanning and processing protocols. Our data set consists of $N = 38,331$ subjects for which white matter hyperintensity binary lesion masks have been gen-

Parameter Estimate: $\hat{\beta}_1$	Bias			Variance			MSE		
N=500	$\lambda = 1$	$\lambda = 2$	$\lambda = 3$	$\lambda = 1$	$\lambda = 2$	$\lambda = 3$	$\lambda = 1$	$\lambda = 2$	$\lambda = 3$
BLESS	-0.0961	-0.0237	-0.0009	0.0014	0.0019	0.0020	0.0106	0.0024	0.0020
BSGLMM	0.0280	0.0129	0.0130	0.0117	0.0080	0.0067	0.0125	0.0082	0.0068
Firth	0.0068	-0.0024	0.0017	0.0562	0.0348	0.0272	0.0563	0.0348	0.0272
N=1,000	$\lambda = 1$	$\lambda = 2$	$\lambda = 3$	$\lambda = 1$	$\lambda = 2$	$\lambda = 3$	$\lambda = 1$	$\lambda = 2$	$\lambda = 3$
BLESS	-0.0031	0.0082	0.0019	0.0010	0.0010	0.0010	0.0010	0.0011	0.0010
BSGLMM	0.0127	0.0106	0.0066	0.0063	0.0045	0.0039	0.0064	0.0046	0.0039
Firth	-0.0002	0.0026	0.0005	0.0271	0.0171	0.0135	0.0271	0.0171	0.0135
N=5,000	$\lambda = 1$	$\lambda = 2$	$\lambda = 3$	$\lambda = 1$	$\lambda = 2$	$\lambda = 3$	$\lambda = 1$	$\lambda = 2$	$\lambda = 3$
BLESS	0.0032	0.0039	-0.0011	0.0002	0.0002	0.0002	0.0002	0.0002	0.0002
BSGLMM	0.0057	0.0054	-0.0006	0.0018	0.0014	0.0012	0.0018	0.0014	0.0012
Firth	0.0022	0.0031	-0.0023	0.0053	0.0034	0.0027	0.0053	0.0034	0.0027

Predictive Performance: \hat{y}	Bias			Variance			MSE		
N=500	$\lambda = 1$	$\lambda = 2$	$\lambda = 3$	$\lambda = 1$	$\lambda = 2$	$\lambda = 3$	$\lambda = 1$	$\lambda = 2$	$\lambda = 3$
BLESS	-0.0078	-0.0052	-0.0032	0.0011	0.0017	0.0018	0.0022	0.0031	0.0034
BSGLMM	-0.0027	-0.0025	-0.0020	0.0002	0.0004	0.0007	0.0002	0.0004	0.0007
Firth	0.0170	0.0140	0.0122	0.0009	0.0016	0.0022	0.0018	0.0032	0.0043
N=1,000	$\lambda = 1$	$\lambda = 2$	$\lambda = 3$	$\lambda = 1$	$\lambda = 2$	$\lambda = 3$	$\lambda = 1$	$\lambda = 2$	$\lambda = 3$
BLESS	-0.0015	0.0007	-0.0013	0.0004	0.0005	0.0007	0.0008	0.0010	0.0012
BSGLMM	-0.0010	-0.0018	-0.0020	0.0001	0.0002	0.0003	0.0001	0.0002	0.0003
Firth	0.0082	0.0082	0.0056	0.0005	0.0008	0.0011	0.0009	0.0016	0.0021
N=5,000	$\lambda = 1$	$\lambda = 2$	$\lambda = 3$	$\lambda = 1$	$\lambda = 2$	$\lambda = 3$	$\lambda = 1$	$\lambda = 2$	$\lambda = 3$
BLESS	-0.0006	0.0000	0.0008	0.0001	0.0001	0.0001	0.0001	0.0002	0.0003
BSGLMM	-0.0004	-0.0008	-0.0001	0.0000	0.0001	0.0001	0.0000	0.0001	0.0001
Firth	0.0010	0.0015	0.0020	0.0001	0.0002	0.0002	0.0002	0.0003	0.0004

Table 2: Evaluation of parameter estimates from the methods, BLESS-VI, BSGLMM and Firth Regression via bias, variance and MSE of the spatially-varying coefficients $\hat{\beta}_1$, and the predictive performance \hat{y} . Improved bias and MSE for prediction for BLESS compared to Firth regression due to selective shrinkage property of BLESS.

erated via the automatic lesion segmentation algorithm BIANCA (Griffanti et al., 2016). The binary lesion maps in subject space are then registered to a common 2mm MNI template across subjects. Each 3D binary image with voxel size $2 \times 2 \times 2 \text{ mm}^3$ and dimensions $91 \times 109 \times 91$ contains a total of 902,629 voxel locations. Our region of interest lies in the white matter tract of the brain and hence the total number of voxels is restricted to $M = 54,728$ by masking the 3D-lesion masks. We are interested in modeling the influence of age on lesion incidence while accounting for the confounding variables sex, head size scaling and the interaction of age and sex (Alfaro-Almagro et al., 2021). The mean age of the participants in our study is 63.6 years (± 7.5 years) and 53.04% of individuals are female (20,332 women).

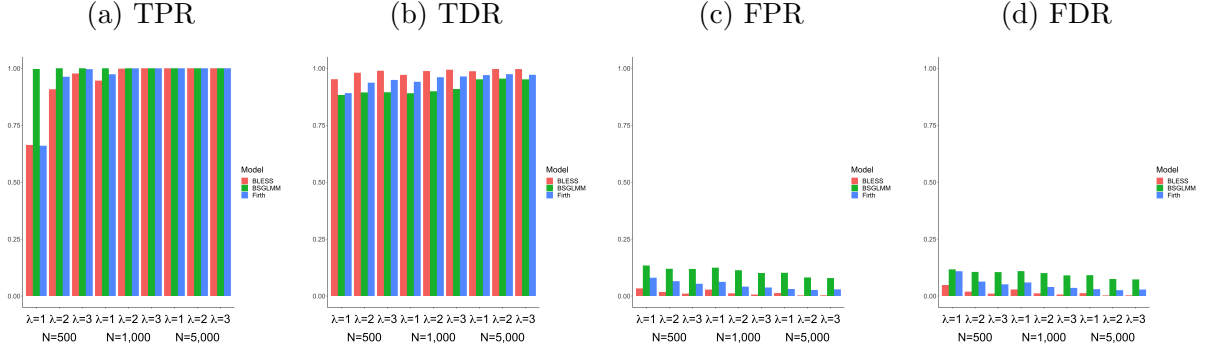


Figure 4: Evaluation of inference results from the methods, BLESS, BSGLMM and Firth Regression (FDR correction at 5%) via True Positive Rate (TPR), True Discovery Rate (TDR), False Positive Rate (FPR) and False Discovery Rate (FDR) for parameter estimate $\hat{\beta}_1$. BLESS outperforms Firth regression and BSGLMM with consistently high TPRs and low FPRs for various sample sizes and base rate intensities.

4.2 Model Estimation

We perform backwards dynamic posterior exploration over $\nu_0 = \{\exp(-10), \dots, \exp(-3)\}$ to help with the optimization of the variational parameters; otherwise, we fit the model identically to the simulation study as described in the previous section. The regularization plot in Figure 5 shows how the age parameter estimates of the detected effects stabilize after the third evaluation of the DPE method. The marginal posterior of the binary latent variable equally captures this trend. The target spike variance value ν_0 remains at the last location of the sequence of spike variances at $\log(\nu_0) = -10$ as showcased by both regularization and marginal plot where negligible coefficients are shrunk almost completely to zero while leaving the larger parameters unaffected by further regularization.

We further estimate BB-BLESS by acquiring $B = 1,500$ bootstrap replicates in which we re-weight the likelihood by drawing Dirichlet weights for every subject with a concentration parameter $\alpha = 1$ and perturb the prior mean of the structured spike-and-slab prior by drawing a “jitter” from $\mathcal{N}(0, \nu_0)$. We initialize the parameters via the results from the DPE procedure and validate the behavior of the annealing-like strategy by examining the regularization and marginal plot in Figure 5. This approximate posterior sampling method remains highly scalable as each optimization can be performed in parallel.

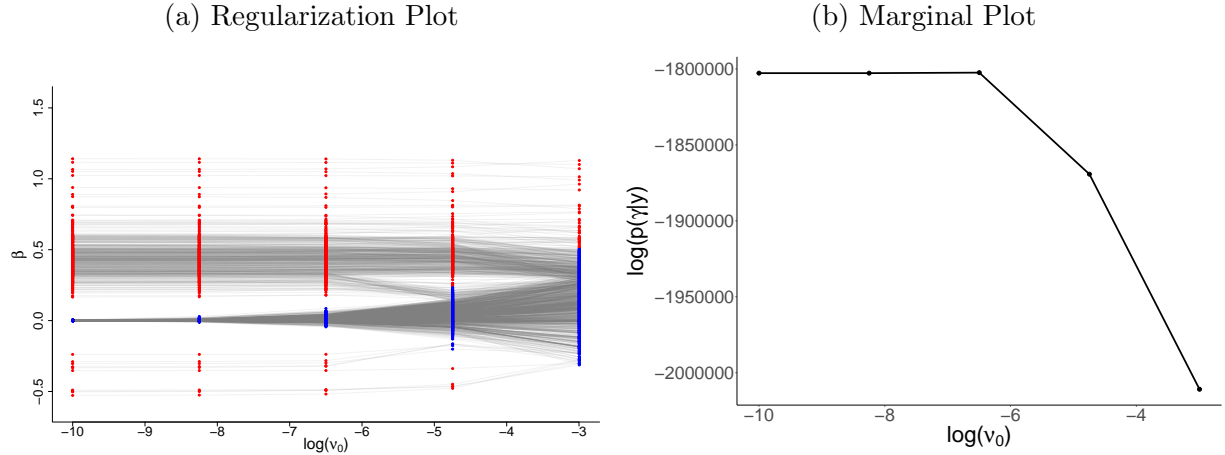


Figure 5: (a) Regularization plot for the age coefficients of an axial slice ($z = 45$, third dimension of the 3D image, plotting all 54,728 coefficients would lead to severe overplotting) (active voxel: red, inactive voxel: blue) and (b) plot of marginal posterior of $\hat{\gamma}$ under $\nu_0 = 0$ over a sequence of equidistant $\nu_0 \in V$ within log-space ($\nu_0 = \{\exp(-10), \dots, \exp(-3)\}$). Parameters stabilize across warm-start initializations. Small effects are shrunk to 0 (blue) and large effects are almost unregularized (red).

4.3 Results

Figure 6 compares the raw age effect size images of our method BLESS, estimated via (a) approximate posterior sampling and (b) variational inference, to (c) the mass-univariate approach Firth regression. It should be noted that we omit the comparison to the other baseline method BSGLMM as the computation of the Bayesian spatial model becomes infeasible due to the large sample size of this study. We highlight how BLESS sufficiently regularizes the negligible age coefficients to zero while leaving the larger effects unaffected. This is a direct consequence of the structured spike-and-slab prior placed on the spatially-varying coefficients. Furthermore, the spatial MCAR prior allows the sparsity dictating parameters within the spike-and-slab prior to borrow strength from their respective neighboring voxels. We further illustrate this behavior by plotting the coefficients of the feature age of the entire 3D effect map of the brain in the scatterplots in Figure 6. The comparison between BLESS-VI and BB-BLESS coefficients again showcases the alignment of posterior mean estimates between the two parameter estimation procedures. The other scatterplots on the other hand capture the induced shrinkage of small effects to zero via BB-BLESS and BLESS-VI while the Firth regression parameter estimates vary for the negligible effects and exhibit non-zero values.

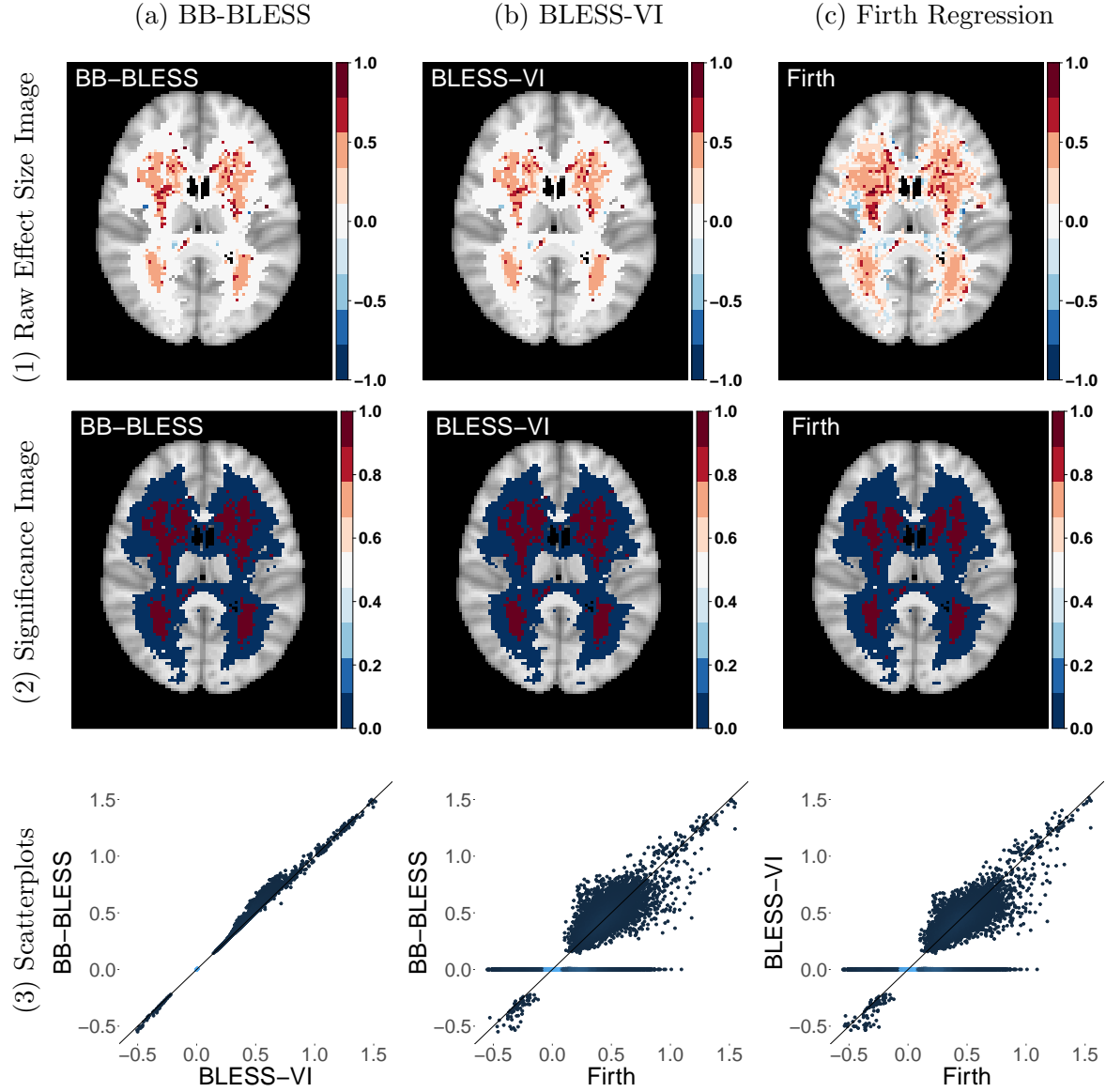


Figure 6: Comparison of results between (a) BB-BLESS, (b) BLESS-VI, and (c) Firth Regression for a single axial slice ($z = 45$, third dimension of 3D image). (1) Spatially-varying age coefficient maps. (2) Thresholded age significance maps where the threshold for BLESS-VI is determined via the probability of inclusion/exclusion $P(\gamma_p(s_j)|\hat{\beta}, \hat{\theta}) \geq 0.5$ and the threshold for BB-BLESS and Firth regression via the test statistic $t = |\hat{\beta}/\hat{\sigma}_{\hat{\beta}}| \geq 1.96$ (significant voxels: red, not significant voxels: blue, FDR-correction applied at 5%). (3) The scatterplots compare the age coefficients for all voxel locations within the 3D image (lighter values indicate higher density of values). The parameter maps estimated via BLESS in (1a) and (1b) exhibit a larger spatial area with values close to 0 compared to Firth in (1c). The scatterplots in (3) show that BLESS regularizes small effects almost completely to 0 compared to Firth.

For inference, we threshold the test statistics of BB-BLESS at a significance level of 5%. In contrast, for BLESS-VI we threshold the posterior probability of inclusion at 0.5 in order to acquire its respective binary significance map. Hence, we exploit variable selection as a means to conduct inference. On the other hand, the mass-univariate approach Firth regression ignores any form of spatial dependence and hence requires the application of a multiple testing correction where we adjust the p-values with a FDR correction (Benjamini and Hochberg, 1995) at a significance level of 5%. The results in Figure 6 indicate a slightly larger extent of spatial activation for BB-BLESS and BLESS-VI compared to Firth regression for a sample size of $N = 2,000$. For the covariate age, in the regression model estimated via Firth regression 10,171 voxels are deemed active based on uncorrected p-values. On the other hand, only 6,278 voxels pass the FDR adjusted threshold whereas in BB-BLESS 8,385 effect locations are detected by utilizing the full posterior to derive test statistics and similarly in BLESS-VI 8,257 effects are detected via simply thresholding the posterior inclusion probabilities.

4.4 Cluster Size Imaging Statistics

Cluster-extent based thresholding is the most commonly used inference technique for statistical maps in neuroimaging studies. By proposing BB-BLESS and hence by sampling from an approximate posterior, we are able to provide novel cluster size based imaging statistics, such as cluster size credible intervals, in addition to reliable uncertainty quantification of the spatially-varying coefficients.

We have shown that the raw age effect size image of the posterior mean for BB-BLESS in Figure 6 obtained as an average over the bootstrap replicates $\bar{\beta}(s_j) = \frac{1}{B} \sum_{b=1}^B \hat{\beta}^{(b)}(s_j)$ for all voxels $j = 1, \dots, M$ is almost identical to BLESS-VI. From our simulation studies, we expect the point estimates from both approximate methods to be identical. However, BB-BLESS is also able to capture the uncertainty of the spatially-varying coefficients more reliably than BLESS-VI. This is important not only for providing uncertainty quantification at a population level but also for making it possible to evaluate the predictive performance via posterior predictive checks, see Section 4.2 of the supplementary material. Moreover, we can use the approximate posterior samples to calculate cluster size based imaging statistics

which require test statistics in their estimation. The statistical map in the top middle part of Figure 7, acquired by the standardization of the raw effects $t(s_j) = \bar{\beta}(s_j)/\sigma_{\beta}(s_j)$ with the posterior standard deviation of each spatially-varying coefficient $\sigma_{\beta}(s_j)$, shows that voxelwise inference based on thresholding the posterior probabilities of inclusion from BLESS-VI at 0.5 is similar to thresholding test statistics at a significance level of $\alpha = 5\%$.

We now highlight two novel cluster size approaches, based on cluster size inference and cluster size mapping, that can be calculated via BB-BLESS. In the first approach we acquire credible intervals of cluster size by utilizing the more accurate posterior standard deviation estimates of BB-BLESS to standardize the bootstrap samples. The resampled statistical maps are then thresholded by a cluster-defining threshold of 2.3 (equivalent to thresholding p-values at a significance level of 0.01) which generates cluster size maps for every bootstrap replicate. We then build a distribution of cluster size by identifying the intersection of each bootstrap cluster with the observed one and recording its respective cluster size. A distribution over cluster sizes for any cluster within the brain allows us to calculate an array of statistical quantities, such as credible intervals of cluster size. In the top right part of Figure 7, we display the cluster size distribution for the largest cluster identified across the brain alongside its 95% credible interval which ranges between a cluster size of 4,063 and 4,265 voxels and contains the observed cluster size value of 4,179 voxels.

In a second cluster size mapping approach, we compute the voxelwise posterior probability of the standardized effect exceeding 2.3. This allows us to create a map of not just large effect but reliably large effect voxels. Comparing the cluster map with the occurrence map provides a measure for the reliability of cluster occurrence at a particular location within the brain. Due to the large spatial extent of the effect of age across the brain and viewing the central axial slice of the 3D maps, almost all voxel locations have a cluster prevalence close to 1. For these locations we then report posterior mean and standard deviation of reliable cluster size at locations where the prevalence of a cluster exceeds 50%.

To summarize, Figure 6 highlights how BLESS is able to reduce the identification of spurious associations for high-dimensional problems by shrinking the model’s negligible coefficients to zero and leaving larger effects unaffected. In the UK Biobank, where we study how age is associated with occurrence of lesions for samples sizes of $N = 2,000$ and $N = 40,000$, age has a very large effect on lesion incidence. However, many studies require methods to identify much subtler risk factors for lesion incidence. The advantage

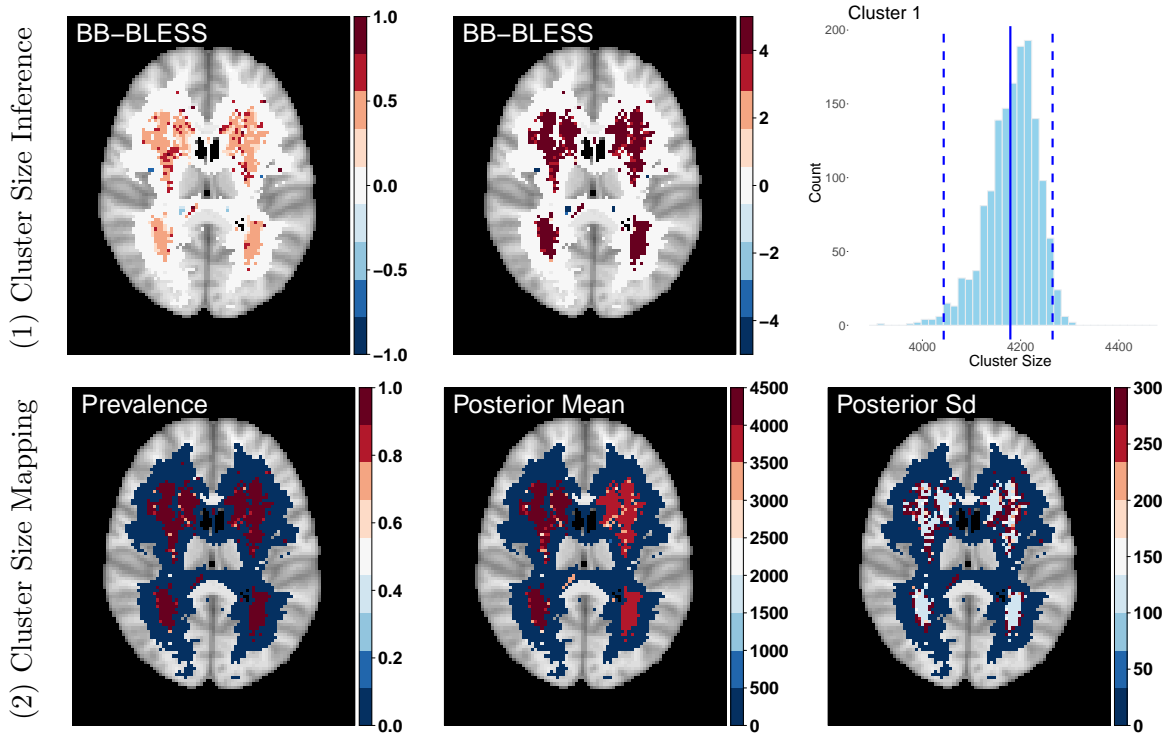


Figure 7: **(1) Cluster Size Inference:** Top left: Raw age effect size image. Top middle: Test statistic map for age effect. Top right: Cluster size distribution for the largest cluster detected by a cluster defining threshold of 2.3 (The solid line indicates the observed cluster size from BLESS-VI and the dashed lines signify the 95% credible interval of cluster size.). **(2) Cluster Size Mapping:** Lower left, middle, right: Prevalence, posterior mean and posterior standard deviation map of cluster size, where the latter two statistics are determined for instances where the prevalence map exceeds a probability of 50%. The prevalence map here indicates that both clusters have reliably large effects with values close to 1.

of BLESS lies in its ability to identify these smaller effects alike with a higher level of specificity and sensitivity compared to Firth regression, a behavior that we have validated in our simulation studies.

In contrast to the mass-univariate approach, we are also able to provide uncertainty estimates of spatially-varying coefficient maps which help in the assessment of spatial associations at a population level. This has the potential to attach risk assessments for identified biomarkers for diseases in an underlying population. Moreover, the posterior variance acquired as a by-product of approximate posterior sampling enables the acquisition of cluster size based imaging statistics. The UK Biobank application for analyzing the effect of age on lesion occurrence only identifies two big clusters, which validates our expectation based around the magnitude of the effect for age. More importantly, BB-BLESS has the unique

advantage to provide us with prevalence statements of cluster size quantities. A spatial map that can aid decisions for follow-up studies, when resources are scarce and a researcher needs to know the reliability of large effect voxels and therefore reliable cluster occurrence across the brain.

5 Discussion

We have proposed a novel Bayesian spatial generalized linear model with a structured spike-and-slab prior for the analysis of binary lesion data. Our main contribution to the neuroimaging community is the development of a scalable version of a Bayesian spatial model that is able to diminish spurious associations by shrinking negligible coefficients to zero, to increase model interpretation via Bayesian variable selection and to provide a model that is also easily extendable to other neuroimaging modalities, such as functional MRI with a continuous response variable.

We further contribute to the area of brain lesion mapping by including a spatial prior in a hierarchical spike-and-slab regression model which provides scalable and voxelwise inference via the process of variable selection. Our method BB-BLESS hereby tackles the known issue of underestimation of posterior variance with variational approaches by approximating posterior sampling via Bayesian bootstrap techniques and a class of jittered spike-and-slab priors. However, due to the increased computational burden of repeated optimizations in BB-BLESS, we aim to provide researchers with computationally faster alternatives for voxelwise inference, which is often the main interest in neuroimaging applications, via BLESS-VI. Our simulation studies show empirically that the sensitivity and specificity of BB-BLESS, where activation is determined via thresholding of test statistics, is very similar to thresholding of posterior inclusion probabilities of BLESS-VI. Hence, one of BLESS’s key advantages remains its scalability to large sample sizes and high-dimensional models via approximate posterior inference in lieu of computationally infeasible MCMC approaches.

We show BLESS’s computational speed with an application to a large scale population health study, the UK Biobank, where we regress lesion incidence on age and various confounds. Additionally, in our cluster size based approaches we provide distributions of cluster size alongside other statistics, such as credible intervals. We also give an indication of the reliability of clusters by treating cluster size as a random variable with a

respective posterior mean and standard deviation that is masked via a prevalence map capturing the occurrence of clusters across resampled maps. The performance of the proposed method with respect to the quality of parameter estimates and inference results has also been extensively validated by our simulation studies in which we compare BLESS to other approaches, such as the mass-univariate Firth regression and the Bayesian spatial model BSGLMM. These studies showed that BLESS generally exhibits very high levels of specificity without sacrificing the sensitivity of the method.

Lastly, we would like to address that in our work we limit the application of BLESS to a clinical application aiming at identifying the association between age and lesion incidence. However, it is a well established finding in the analysis of white matter hyperintensities that age is one of the strongest predictors of lesion incidence (Wardlaw et al., 2013). Therefore, the study of more subtle risk factors for disease poses an interesting future research direction, as for example the further exploration of the cognitive impact of cerebrovascular risk-related white matter hyperintensities (Veldsman et al., 2020).

Acknowledgments

The authors gratefully acknowledge the following funding sources: **AM** is a student of the EPSRC StatML CDT (EP/S023151/1) and receives funding from the Oxford-Radcliffe scholarship and Novartis. **TEN** receives funding from the Wellcome Trust (100309/Z/12/Z) and NIH grant 1R01DA048993. **CH** is supported by The Alan Turing Institute, Health Data Research UK, the Medical Research Council UK, the EPSRC through the Bayes4Health grant EP/R018561/1, and AI for Science and Government UKRI. **HG** is supported by Novartis. We would also like to thank the participants of the UK Biobank for their contribution to the study which was conducted under application number 34077 and 8107.

References

- James H. Albert and Siddhartha Chib. Bayesian analysis of binary and polychotomous response data. *JASA*, 88(422):669–679, 1993.
- Fidel Alfaro-Almagro, Jenkinson M., Bangerter N.K., Andersson J.L.R., Griffanti L., Douaud G., Sotiropoulos S.N., Jbabdi S., Hernandez-Fernandez M., Vallee E., Vidaurre D., Webster M., McCarthy P., Rorden C., Daducci A., Alexander D.C., Zhang H., Dragonu I., Matthews P.M., Miller K.L., and Smith S.M. Image processing and quality control for the first 10,000 brain imaging datasets from UK Biobank. *NeuroImage*, 166: 400–424, 2 2018.

- Fidel Alfaro-Almagro, Paul McCarthy, Soroosh Afyouni, Jesper L.R. Andersson, Matteo Bastiani, Karla L. Miller, Thomas E. Nichols, and Stephen M. Smith. Confound modelling in UK Biobank brain imaging. *NeuroImage*, 224:117002, 1 2021.
- Michael Riis Andersen. Bayesian Inference for Spatio-temporal Spike-and-Slab Priors. 18: 1–58, 2017.
- Michael Riis Andersen, Ole Winther, and Lars Kai Hansen. Bayesian inference for structured spike and slab priors. *Advances in Neural Information Processing Systems*, 2: 1745–1753, 2014.
- Maria M. Barbieri, James O. Berger, Edward I. George, and Veronika Ročková. The Median Probability Model and Correlated Variables. *Bayesian Analysis*, 16(4):1085 – 1112, 2021.
- Yoav Benjamini and Yosef Hochberg. Controlling the false discovery rate: A practical and powerful approach to multiple testing. *J R Stat Soc Ser B*, 57(1):289–300, 1995.
- Julian Besag. Spatial interaction and the statistical analysis of lattice systems. *J R Stat Soc Ser B*, 36(2):192–225, 1974.
- Julian Besag. On the statistical analysis of dirty pictures. *J R Stat Soc Ser B*, 48(3): 259–302, 1986.
- Julian Besag. Towards Bayesian image analysis. *Journal of Applied Statistics*, 20(5-6): 107–119, 1993.
- Christopher M. Bishop. *Pattern Recognition and Machine Learning*. 2006.
- David M. Blei, Alp Kucukelbir, and Jon D. McAuliffe. Variational Inference: A Review for Statisticians. *JASA*, 112(518):859–877, 2017.
- D. Brook. On the distinction between the conditional probability and the joint probability approaches in the specification of nearest-neighbour systems. *Biometrika*, (51):481–483, 1964.
- Peter Carbonetto and Matthew Stephens. Scalable variational inference for Bayesian variable selection in regression, and its accuracy in genetic association studies. *Bayesian Analysis*, 7(1):73–108, 2012.
- Carlos M. Carvalho, Nicholas G. Polson, and James G. Scott. Handling sparsity via the horseshoe. volume 5 of *PMLR*, pages 73–80, 2009.
- Arnaud Charil, Alex P Zijdenbos, Jonathan Taylor, Cyrus Boelman, Keith J Worsley, Alan C Evans, and Alain Dagher. Statistical mapping analysis of lesion location and neurological disability in multiple sclerosis: application to 452 patient data sets. *NeuroImage*, 19(3):532 – 544, 2003.
- S. Debetto and H. S. Markus. The clinical importance of white matter hyperintensities on brain magnetic resonance imaging: systematic review and meta-analysis. *BMJ*, 341, 2010.
- David Firth. Bias reduction of maximum likelihood estimates. *Biometrika*, 80(1):27–38, 1993.
- Edwin Fong, Simon Lyddon, and Chris Holmes. Scalable Nonparametric Sampling from Multimodal Posteriors with the Posterior Bootstrap. *PMLR*, 97:1952–1962, 2019.
- K. J. Friston, A. Holmes, J. B. Poline, C. J. Price, and C. D. Frith. Detecting activations in PET and fMRI: levels of inference and power. *NeuroImage*, 4:223–235, 1996.

- Tian Ge, Nicole Müller-Lenke, Kerstin Bendfeldt, Thomas E. Nichols, and Timothy D. Johnson. Analysis of multiple sclerosis lesions via spatially varying coefficients. *The Annals of Applied Statistics*, 8(2):1095 – 1118, 2014.
- Alan E. Gelfand and Penelope Vounatsou. Proper multivariate conditional autoregressive models for spatial data analysis. *Biostatistics*, 4(1):11–15, 2003.
- Edward I. George and Robert E. McCulloch. Variable Selection via Gibbs Sampling. *JASA*, 88(423):881–889, 1993.
- Edward I. George and Robert E. McCulloch. Approaches for Bayesian Variable Selection. *Statistica Sinica*, 7(2):339–373, 1997.
- Ludovica Griffanti, G. Zamboni, A. Khan, L. Li, G. Bonifacio, V. Sundaresan, U. G. Schulz, W. Kuker, M. Battaglini, P. M. Rothwell, and M. Jenkinson. BIANCA (Brain Intensity AbNormality Classification Algorithm): A new tool for automated segmentation of white matter hyperintensities. *NeuroImage*, 141:191–205, 2016.
- Ludovica Griffanti, M. Jenkinson, S. Suri, E. Zsoldos, A. Mahmood, N. Filippini, C. E. Sexton, A. Topiwala, C. Allan, M. Kivimäki, A. Singh-Manoux, K. P. Ebmeier, C. E. Mackay, and G. Zamboni. Classification and characterization of periventricular and deep white matter hyperintensities on MRI: A study in older adults. *NeuroImage*, 170:174–181, 2018.
- Daniel Hernández-Lobato, J. Miguel Hernández-Lobato, and P. Dupont. Generalized spike-and-slab priors for Bayesian group feature selection using expectation propagation. *JMLR*, 14:1891–1945, 2013.
- Tommi S. Jaakkola and Michael I. Jordan. Bayesian parameter estimation via variational methods. *Statistics and Computing*, 10(1):25–37, 2000.
- Valen E. Johnson and David Rossell. On the use of non-local prior densities in Bayesian hypothesis tests. *J R Stat Soc Ser B*, 72(2):143–170, 2010.
- M. I. Jordan, Z. Ghahramani, T. S. Jaakkola, and L. K. Saul. An introduction to variational methods for graphical models. *Mach. Learn.*, 37(2):183–233, 1999.
- Ioannis Kosmidis. *brglm2: Bias Reduction in Generalized Linear Models*, 2021. URL <https://CRAN.R-project.org/package=brglm2>. R package version 0.8.0.
- Ioannis Kosmidis, E.C. Kenne Pagui, and N. Sartori. Mean and median bias reduction in generalized linear models. *Stat Comput*, 30:43–59, 11 2020.
- Leonie Lampe, R. Zhang, F. Beyer, S. Huhn, S. Kharabian Masouleh, S. Preusser, P. Bazin, M. L. Schroeter, A. Villringer, and A. V. Witte. Visceral obesity relates to deep white matter hyperintensities via inflammation. *Annals of Neurology*, 85(2):194–203, 2019.
- Fan Li and Nancy R. Zhang. Bayesian variable selection in structured high-dimensional covariate spaces with applications in genomics. *JASA*, 105(491):1202–1214, 2010.
- Simon Lyddon, S. Walker, and C. Holmes. Nonparametric learning from Bayesian models with randomized objective functions. *NeurIPS 2018*, pages 2075–2085, 2018.
- K. V. Mardia. Multi-dimensional multivariate Gaussian Markov random fields with application to image processing. *Journal of Multivariate Analysis*, 24(2):265–284, 1988.
- K. Miller, F. Alfaro-Almagro, N. Bangerter, and D. L. Thomas. Multimodal population brain imaging in the UK Biobank prospective epidemiological study. *Nature Neuroscience*, (19):1523–1536, 2016.

- Thomas E Minka. Expectation Propagation for Approximate Bayesian Inference. 2001. doi: 10.5555/2074022.2074067.
- T. J. Mitchell and J. J. Beauchamp. Bayesian variable selection in linear regression. *JASA*, 83(404):1023–1032, 1988.
- Michael A. Newton and Adrian E. Raftery. Approximate Bayesian Inference with the Weighted Likelihood Bootstrap. *J R Stat Soc Ser B*, 56(1):3–26, 1994.
- Michael A. Newton, Nicholas G. Polson, and Jianeng Xu. Weighted Bayesian bootstrap for scalable posterior distributions. *Canadian Journal of Statistics*, 49(2):421–437, 2021.
- Lizhen Nie and Veronika Ročková. Bayesian Bootstrap Spike-and-Slab LASSO. *JASA*, 0(0):1–16, 2022.
- Juho Piironen and Aki Vehtari. Sparsity information and regularization in the horseshoe and other shrinkage priors. *Electronic Journal of Statistics*, 11(2):5018 – 5051, 2017.
- J. B. Poline and B. M. Mazoyer. Analysis of individual positron emission tomography activation maps by detection of high signal-to-noise-ratio pixel clusters. *Journal of Cerebral Blood Flow and Metabolism*, 13:425–437, 6 1993.
- Niels D. Prins and Philip Scheltens. White matter hyperintensities, cognitive impairment and dementia: an update. *Nature Reviews Neurology*, 11(3):157–165, 2015.
- Veronika Ročková and Edward I. George. EMVS: The EM approach to Bayesian variable selection. *JASA*, 109(506):828–846, 2014.
- Veronika Ročková and Edward I. George. The Spike-and-Slab LASSO. *JASA*, 113(521):431–444, 2018.
- E. Rostrup, A.A. Gouw, H. Vrenken, E.C.W. van Straaten, S. Ropele, L. Pantoni, D. Inzitari, F. Barkhof, and G. Waldemar. The spatial distribution of age-related white matter changes as a function of vascular risk factors—Results from the LADIS study. *NeuroImage*, 60(3):1597–1607, 2012.
- Donald B. Rubin. The Bayesian Bootstrap. *The Annals of Statistics*, 9(1):130 – 134, 1981.
- Francesco C. Stingo, Yian A. Chen, Marina Vannucci, Marianne Barrier, and Philip E. Mirkes. A Bayesian graphical modeling approach to microRNA regulatory network inference. *The Annals of Applied Statistics*, 4(4):2024 – 2048, 2010.
- Michele Veldsman, Petya Kindalova, Masud Husain, Ioannis Kosmidis, and Thomas E. Nichols. Spatial distribution and cognitive impact of cerebrovascular risk-related white matter hyperintensities. *NeuroImage: Clinical*, 28:102405, 2020.
- Martin J. Wainwright and Michael I. Jordan. Graphical models, exponential families, and variational inference. *Foundations and Trends in Machine Learning*, 1(1–2):1–305, 2008.
- JM Wardlaw, EE Smith, GJ Biessels, and C Cordonnier. Neuroimaging standards for research into small vessel disease and its contribution to ageing and neurodegeneration. *Lancet Neurol.*, 12(8):822–838, 2013.
- JM Wardlaw, MC Valdés Hernández, and S Muñoz-Maniega. What are white matter hyperintensities made of? Relevance to vascular cognitive impairment. *J. Am. Heart Assoc.*, 4(6), 2015.
- Choong Wan Woo, Anjali Krishnan, and Tor D. Wager. Cluster-extent based thresholding in fMRI analyses: Pitfalls and recommendations. *NeuroImage*, 91:412–419, 5 2014.
- Yuling Yao, Aki Vehtari, Daniel Simpson, and Andrew Gelman. Yes, but did it work?: Evaluating variational inference. *PMLR*, 80:5581–5590, 2018.